Atomic oxygen in the mesosphere and lower thermosphere derived from SABER: Algorithm theoretical basis and measurement uncertainty

Martin G. Mlynczak,[1] Linda A. Hunt,[2] Jeffrey C. Mast,[2] B. Thomas Marshall,[3] James M. Russell III,[4] Anne K. Smith,[5] David E. Siskind,[6] Jeng-Hwa Yee,[7] Christopher J. Mertens,[1] F. Javier Martin-Torres,[8] R. Earl Thompson,[3] Douglas P. Drob,[6] and Larry L. Gordley[3]

[1] Atomic oxygen (O) is a fundamental component in chemical aeronomy of Earth's mesosphere and lower thermosphere region extending from approximately 50 km to over 100 km in altitude. Atomic oxygen is notoriously difficult to measure, especially with remote sensing techniques from orbiting satellite sensors. It is typically inferred from measurements of the ozone concentration in the day or from measurements of the Meinel band emission of the hydroxyl radical (OH) at night. The Sounding of the Atmosphere using Broadband Emission Radiometry (SABER) instrument on the NASA Thermosphere-Ionosphere-Mesosphere Energetics and Dynamics (TIMED) satellite measures OH emission and ozone for the purpose of determining the O-atom concentration. In this paper, we present the algorithms used in the derivation of day and night atomic oxygen from these measurements. We find excellent consistency between the day and night O-atom concentrations from daily to annual time scales. We also examine in detail the collisional relaxation of the highly vibrationally excited OH molecule at night measured by SABER. Large rate coefficients for collisional removal of vibrationally excited OH molecules by atomic oxygen are consistent with the SABER observations if the deactivation of OH(9) proceeds solely by collisional quenching. An uncertainty analysis of the derived atomic oxygen is also given. Uncertainty in the rate coefficient for recombination of O and molecular oxygen is shown to be the largest source of uncertainty in the derivation of atomic oxygen day or night.

1. Introduction

[2] A fundamental problem in the chemical aeronomy of the Earth's mesosphere and lower thermosphere (MLT)

[1]NASA Langley Research Center, Hampton, Virginia, USA.
[2]Science Systems and Applications Inc., Hampton, Virginia, USA.
[3]G & A Technical Software, Newport News, Virginia, USA.
[4]Hampton University, Hampton, Virginia, USA.
[5]National Center for Atmospheric Research, Boulder, Colorado, USA.
[6]Naval Research Laboratory, Washington, District of Columbia, USA.
[7]Johns Hopkins University Applied Physics Laboratory, Laurel, Maryland, USA.
[8]Centro de Astrobiologia (CSIC-INTA), Madrid, Spain.

Corresponding author: Corresponding author: M. G. Mlynczak, NASA Langley Research Center, Hampton, VA, USA. (m.g.mlynczak@nasa.gov)

region is the determination of the atomic oxygen (O) concentration. O plays a critical role in the photochemistry and energy balance of the upper MLT, which we define here as the atmosphere between 10^{-1} hPa and 10^{-4} hPa or approximately 65–105 km in altitude. Specifically, O is generated through photolysis of molecular oxygen by UV radiation. O plays a fundamental role in chemical and radiant energy budgets of the MLT region. Exothermic chemical reactions throughout the MLT are fueled by atomic oxygen both day and night [*Mlynczak and Solomon*, 1993]. In addition, atomic oxygen is also important in the radiant cooling of the MLT as collisions between O and CO_2 excite the vibrational quantum states of CO_2, which then radiate in the IR, cooling the MLT. Thus, accurate knowledge of the O-atom concentration is essential to understanding the photochemistry and energy budget of the MLT.

[3] Measuring atomic oxygen in the upper MLT is very difficult with either in situ techniques or remote sensing techniques from orbiting satellites. As an atomic species, O has no vibration-rotation spectra, but rather, it has two fine

structure lines: one centered near 63 µm, the other near 145 µm. The 63 µm line is optically thick and is not observable in the upper MLT from space [e.g., *Grossmann et al.*, 2000]. The 63 µm line has been measured by rocket-borne instruments [e.g., *Grossmann and Vollmann*, 1997] and by high-altitude balloons [*Mlynczak et al.*, 2004]. The 145 µm line is optically thin but requires complex technology to observe from a satellite. Thus, there are no global observations of the O-atom concentration in the MLT obtained from direct observations of radiant emission from O itself.

[4] Prior to the modern satellite era that began with the launch of the Upper Atmosphere Research Satellite in 1991, atomic oxygen was often measured in situ by suborbital rockets using resonance lamp techniques [e.g., *Dickinson et al.*, 1974, 1980], airglow techniques [e.g., *Good*, 1976], or a combination of both [e.g., *Ulwick et al.*, 1987]. There was substantial debate in the 1980s as to the value of the peak concentration of atomic oxygen in the mesopause region. This debate was due in part to the challenges associated with the measurements including knowledge of the rates and mechanisms of the airglow and optical contamination and shock effects from the rockets carrying the payloads. Reported peak concentration values from different techniques spanned an order of magnitude, from $10^{11}\,\mathrm{cm}^{-3}$ to $10^{12}\,\mathrm{cm}^{-3}$ [*Llewellyn*, 1988], although *Siskind and Sharp* [1991] argued that some of the discrepancy could be mitigated with a better understanding of airglow variability. A number of rocket flights and theoretical studies in the 1980s investigated the OH airglow in great detail [e.g., *McDade and Llewellyn*, 1987; *McDade et al.*, 1987; *McDade*, 1991]. A fundamental question addressed by these measurements and studies was the mechanisms by which collisional relaxation of highly vibrationally excited OH proceeded. As will be shown in section 4, these questions are still relevant today in the interpretation of the Sounding of the Atmosphere using Broadband Emission Radiometry (SABER) OH data in light of recent laboratory measurements of quenching of OH(9) in collisions with atomic oxygen.

[5] Today, the general approach to determining the O-atom concentration in the MLT is to infer it from satellite measurements of related species or emission features. Atomic oxygen is typically inferred at night from measurements of radiative emission from the Meinel bands of the hydroxyl (OH) molecule. This technique was developed by *Good* [1976] and assumes that the production of ozone (O_3) by recombination of O and O_2 is balanced by reaction of O_3 with atomic hydrogen, the latter reaction generating the OH Meinel band emission. The O derived from this technique is an inference and relies on the assumption of photochemical steady state and on the provision of physical quenching rates, radiative lifetimes, and reaction rate coefficients for the highly vibrationally excited states of the OH molecule observed by instruments such as SABER. These rates and rate coefficients have been the subject of debate over the years, and they represent a large source of uncertainty in the derivation of atomic oxygen from OH Meinel band emission measurements. We will also show that the rate coefficient for the recombination of O and O_2 is a major source of uncertainty in the derivation of atomic oxygen. In the daytime, O may be inferred from observations of ozone by assuming that the photolysis of O_3 is balanced by recombination of O and O_2. This yields a simple expression involving the ozone Hartley band

photolysis rate and the recombination rate coefficient for O and O_2. Temperature and pressure (for number density) are also required.

[6] The SABER instrument [*Russell et al.*, 1999] on the Thermosphere-Ionosphere-Mesosphere Energetics and Dynamics (TIMED) satellite has been observing OH emission and ozone in the MLT since 2002. SABER observations of daytime ozone and night OH emission are used in the derivation of atomic oxygen. Several papers have appeared in the literature describing the observed properties of O from SABER measurements [e.g., *Marsh et al*; 2006; *Smith et al.*, 2010; *Xu et al.*, 2012]. In this paper, we describe the specific algorithms and derivations of atomic oxygen both day and night from the SABER measurements. We first demonstrate the excellent quality of the SABER radiance data on which these retrievals/derivations are based and then discuss the day and night algorithms in detail. We then consider the specific collisional processes and rate coefficients that describe the physical quenching of the highly excited OH molecule. We will also show that the recently reported large rate coefficients for the quenching of highly vibrational excited OH by O atoms are consistent with the SABER observations if the deactivation of OH(9) proceeds by a single quantum step. Lastly, we examine the uncertainty of the derived atomic oxygen and show that the estimated uncertainty is ~25%–30%.

[7] We finally assess concentrations from the perspective of their absolute values and also from the rates of heating due to the release of chemical potential energy from the recombination of O. On approximately annual time scales, the rates of chemical heating must be comparable to the radiative cooling; otherwise, the atmosphere would continue to warm perpetually. In essence, long-term energy balance places a strong constraint on the global average atomic oxygen concentration. A companion paper, *Mlynczak et al.* [2013] (hereafter Paper 2), examines in detail radiative constraints on the atomic oxygen concentration in the upper MLT.

1.1. Data Preparation and Screening

[8] All of the algorithms and results reported here are for version 1.07 of the SABER data set and will be used in the upcoming version 2 of the data set. Profiles of pressure, altitude, temperature, ozone volume mixing ratio (derived from the 9.6 µm channel), and OH volume emission rate (at 2.0 µm) are extracted from the SABER level 2A data file. A small number of profiles are rejected if more than 20% of the possible data points are missing and because of an anomaly that results in assignment of anomalously high altitudes to the lowest pressure level (10^{-4} hPa) considered herein. In all, less than 1% of the data are rejected.

[9] The profiles are interpolated from the native SABER pressure registration grid (which is different for every profile) to a standard grid that covers three decades in pressure, 0.1–10^{-4} hPa, with 10 pressure levels per decade, 31 levels overall, from approximately 65 km to 105 km. The profile is assigned a solar zenith angle, latitude, and longitude corresponding to that at 90 km altitude.

[10] For the daytime atomic oxygen calculation, profiles with a solar zenith angle less than 85° are selected from this set. The O_3 volume mixing ratio is screened to exclude values less than 10^{-9} or greater than 5.0×10^{-5}. Profiles used at night have a solar zenith angle greater than 95°. At

night, the OH volume emission rates are screened to have a minimum value of 5.0×10^{-10} ergs $cm^{-3} s^{-1}$ which corresponds to a volume emission rate nearly equal to the noise value. The derived atomic oxygen concentration values (day or night) are screened to be positive and less than $1.25 \times 10^{12} cm^{-3}$, which corresponds to a heating rate for the recombination of atomic oxygen in excess of 28 K/d. This screening is based on consideration of the total energy balance and is discussed in more detail in section 4 (and in Paper 2). This screening results in rejection of less than 2% of all data between 0.01 and 0.0001 hPa.

[11] Daily (i.e., 24 h) averages are determined by binning the day's data by hour and then averaging over the hour bins that contain data to get the daily average value. Annual averages are then calculated for each of sixteen 11° latitude bins for each pressure grid level over a SABER yaw year, i.e., for the six 2 month yaw cycles from mid-January of 1 year to mid-January of the next. Yaw years from 2004 to 2011 were processed. "Global" annual averages are calculated from 55°S to 55°N since this is the region that is viewed continuously by SABER in every yaw period. The global average calculation uses cosine latitude weighting, so each bin's value is proportional to its area. In this paper, all global averages are taken from 55°S to 55°N and cover 82% of total atmospheric area.

2. Derivation of Daytime Atomic Oxygen

[12] In the daytime, atomic oxygen is derived in the mesosphere and lower thermosphere assuming that ozone is in steady state. Specifically, the assumption is that production of ozone by recombination is balanced by photolysis in the Hartley band. The lifetime of ozone in the upper MLT is about 120 s against photolysis, so this assumption appears quite valid for the daytime. The steady state balance is given simply by the following:

$$k_2 [O] [O_2] [M] \quad = \quad J [O_3] \quad (1)$$

[13] In equation (1), k_2 is the recombination rate coefficient; O, O_2, O_3, and M are the concentrations of atomic oxygen, molecular oxygen, ozone, and the total number density, respectively. J is the photolysis rate (s^{-1}) of the Hartley band. Atomic oxygen is derived from equation (1) using O_3 measured at 9.6 μm from SABER. Molecular oxygen and the total number density are derived from SABER pressure and temperature data using the ideal gas law and an O_2 volume mixing ratio of 0.21. SABER temperatures are used in evaluating k_2, taken as $6.0 \times 10^{-34} (300/T)^{2.4}$ [Sander et al., 2011].

[14] Daytime atomic oxygen is derived over the range of pressures from 0.1 to 0.0001 hPa, approximately 65–105 km altitude. The photolysis rate J is computed on a daily basis using the solar irradiance measured by the SORCE satellite [Rottman, 2005]. Over the range of pressures here, the photolysis rate is taken to be constant with altitude at the exoatmospheric rate. Simulations showed that even at large solar zenith angles, there is not sufficient ozone to reduce the photolysis rate from the exoatmospheric value. The photolysis rate is computed from the product of the solar irradiance and the ozone Hartley band cross sections between 176.5 and 350.5 nm.

[15] Atomic oxygen is derived using ozone retrieved from SABER measurements of IR emission from ozone itself at

9.6 μm. SABER also observes the 1.27 μm molecular oxygen dayglow emission for the derivation of daytime ozone [Mlynczak et al., 2007]. The 9.6 μm ozone is used in the derivation of atomic oxygen because it is a direct measure of ozone and is valid at all local times throughout the day from sunrise to sunset. The 1.27 μm emission has a radiative lifetime of approximately 75 min and does not provide a representative measure of ozone until 2–3 h after sunrise.

[16] A separate paper describing the SABER ozone algorithm for 9.6 μm emission is in preparation, but we will summarize the salient points here. Ozone emission is observed in a relatively narrow band pass from 1010 to 1150 cm^{-1}. This interval was chosen to emphasize measurement of emission from the fundamental (001-000) band in asymmetric stretch (v_3) mode of ozone so as to minimize emission from the higher-lying hot bands of ozone. In the MLT, the entire v_3 manifold departs from local thermodynamic equilibrium (LTE). The hot bands are chemically pumped as was discovered from analysis of ozone measurements made by the Limb Infrared Monitor of the Stratosphere (LIMS) instrument [Solomon et al., 1986]. The spectral band pass for SABER is substantially narrower than used on LIMS to minimize uncertainty in the retrieved ozone from the non-LTE emission from the hot bands. Shown in Figure 1 are the relative spectral response functions for the SABER and LIMS ozone channels.

[17] The retrieval of ozone requires a statistical equilibrium model of the vibrational states in the ground electronic state of the ozone molecule. The SABER ozone vibrational temperature model is drawn from Mlynczak and Drayson [1990a, 1990b] and Martin-Torres [1999]. This model is used to compute the vibrational temperatures of the bands of ozone that emit within the SABER band pass. The SABER model includes spontaneous emission of radiation, chemical pumping, collisional excitation and quenching with N_2, O_2, and O, and radiative excitation in the v_3 fundamental band using the computationally efficient approach defined by Mlynczak and Drayson [1991]. The collisional quenching rates for N_2 and O_2 were developed in Martin-Torres' thesis from the work of Menard-Bourcin et al. [1991]. The quenching rate for atomic oxygen was taken from West et al. [1976]. Over 130 vibrational states are in the SABER model; however, most of the ozone emission in the SABER band pass comes from the v_3 fundamental. An additional source of IR radiance in the SABER band pass is due to one of the two IR "laser bands" of CO_2 [Mlynczak and Drayson, 1990b]. This emission is taken into account in the ozone retrieval using vibrational temperatures computed for CO_2 in the SABER temperature retrieval algorithm. The ozone vibrational temperatures are independent of the ozone abundance because the radiative transfer in the mesosphere is in the weak line limit. Physical quenching of the v_3 manifold by atomic oxygen is included using atomic oxygen concentrations provided by the MSIS model. The vibrational temperatures are computed independent of the ozone abundance and are then used in the retrieval of ozone concentrations from the measured limb radiance profiles.

[18] Figure 2 shows individual limb radiance profiles at 9.6 μm measured by SABER from 0.1 hPa to 0.0001 hPa during the daytime portion of a single orbit on 22 September 2004. The noise equivalent radiance for this channel is specified by the vertical dashed line. The figure shows the high signal to noise of the SABER ozone channel, exceeding a
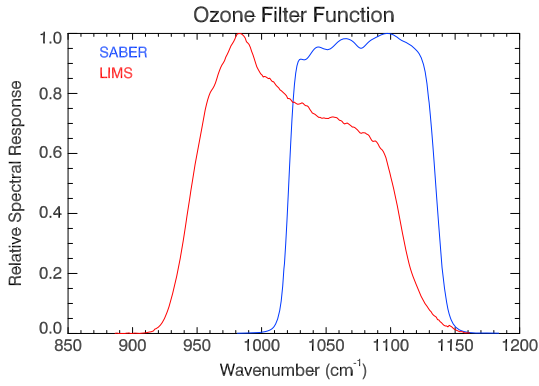
Figure 1. SABER and LIMS relative spectral response functions for their respective ozone channels.

Figure 3. Daytime zonal mean ozone volume mixing ratios (parts per million by volume) for 22 September 2004 derived from SABER at 9.6 μm.

factor of 100 in the lower mesosphere and exceeding a factor of ~20 at 90 km. The signal-to-noise ratio goes to 1 at approximately 100 km altitude. SABER retrieves daytime ozone over this entire range of altitudes for each measured radiance profile. Note that the SABER vertical coordinate is pressure and all plots are shown with pressure on the ordinate. An approximate altitude is shown on the right vertical axis. The vertical resolution of the SABER ozone data is approximately 2 km.

[19] Shown in Figure 3 is an example of the SABER daytime ozone, specifically the daytime zonal mean ozone volume mixing ratios (in parts per million by volume (ppmv)) measured on 22 September 2004. The expected minimum in the middle mesosphere between 70 and 80 km is present as is the secondary maximum near 90 km with a peak mixing ratio of about 1.2 ppmv.

[20] To derive the daytime atomic oxygen, we apply equation (1) as described above. The SABER data quality (i.e., the high signal to noise) enables the derivation of atomic oxygen for each measured profile of daytime ozone. These profiles may then be further averaged spatially and temporally as desired. Shown in Figure 4 is the daytime zonal average atomic oxygen concentration corresponding to the ozone measurements for 22 September 2004 shown in Figure 3. The concentration units are in $10^{11}\,\mathrm{cm}^{-3}$, so a value of 7 in the plot corresponds to a

concentration of $7 \times 10^{11}\,\mathrm{cm}^{-3}$. The peak atomic oxygen concentration occurs at ~95 km near the equator on this day. The daytime zonal annual average atomic oxygen is shown in Figure 5. The peak atomic oxygen concentration is $6 \times 10^{11}\,\mathrm{cm}^{-3}$ and occurs in the vicinity of 95 km. The annual daytime atomic oxygen shows little variation with latitude, and this is taken to be indicative of very little meridional ozone variation when averaged over a year.

3. Night Atomic Oxygen from OH Emission

[21] The SABER instrument measures limb radiance from the OH molecule in two channels: one located near 2.0 μm and one located near 1.6 μm. The 2.0 μm channel was chosen specifically to measure the OH(9–7) and OH(8–6) band emission so as to observe directly the rate of reaction of H and O_3 [*Mlynczak*, 1999] and to facilitate the derivation of atomic oxygen by minimizing the number of parameters used in the modeling of the OH emission. The 1.6 μm channel observes emission from OH in the middle of its vibrational manifold. The purpose of the 1.6 μm channel is to enable observation of energy flow through the OH molecule during its formation so as to better understand the heating efficiency due to the reaction of H and O_3, which is the single largest source of heat near the Earth's mesopause [*Mlynczak and*
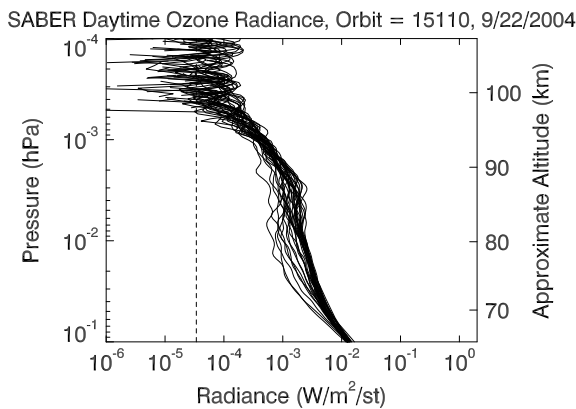

Figure 2. SABER daytime 9.6 μm limb radiances for one orbit measured on 22 September 2004. The vertical dashed line is the noise equivalent radiance level for this channel.
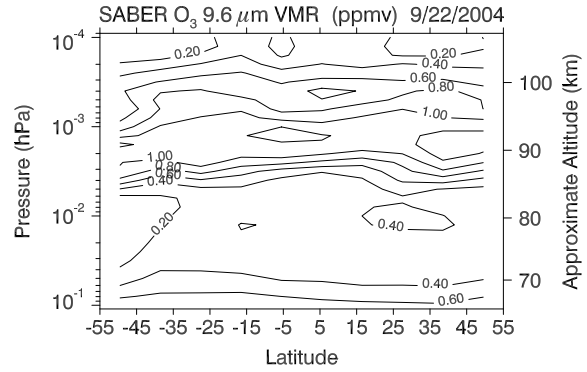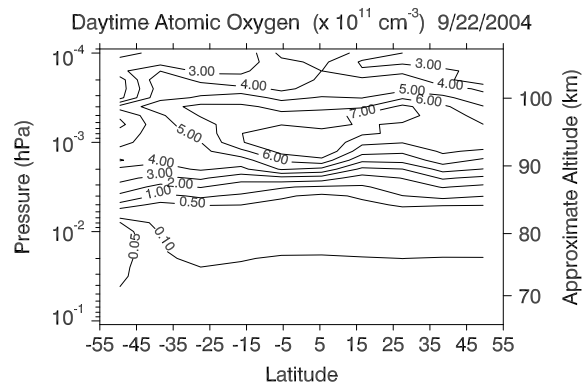

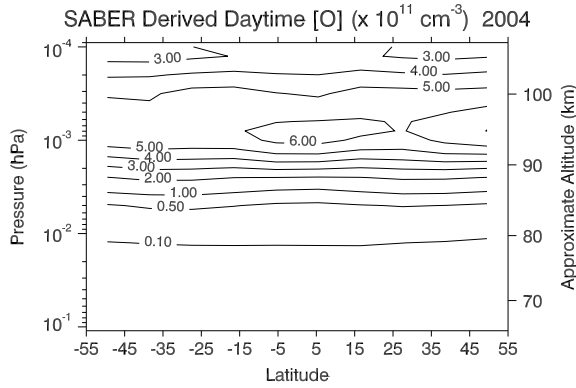**Figure 4.** SABER-derived daytime atomic oxygen on 22 September 2004 from the ozone concentrations shown in Figure 3.

Figure 5. Daytime zonal annual average concentrations of atomic oxygen for 2004 derived from measurements of ozone at 9.6 μm.

Figure 7. SABER night OH 2.0 μm limb radiance profiles for one orbit on 22 September 2004. The vertical dashed line is the noise equivalent radiance level for this channel.

Solomon, 1991]. For the derivation of atomic oxygen, we use only the 2.0 μm channel measurements.

[22] Shown in Figure 6 is the SABER OH 2.0 μm channel relative spectral response filter function. Also shown are the normalized line strengths and line positions for the 9–7, 8–6, and 7–5 bands. The 7–5 band contributes only a few percent to the measured SABER OH emission and is not considered in the SABER atomic oxygen algorithm. Figure 7 shows one orbit of night limb radiance measurements in the SABER 2.0 μm channel recorded on 22 September 2004. The vertical dashed line indicates the noise equivalent radiance level. The SABER OH 2.0 μm channel has a very high signal-to-noise ratio, ranging from a factor of 100 to 1000 at the peak. This exceptional measurement precision facilitates the inversion of each individual limb radiance profile to OH volume emission rates from which the O-atom concentrations are derived at night. Examination of Figure 7 shows that the 2.0 μm emission measured by SABER extends to well above 100 km with a single scan signal-to-noise ratio of greater than 10 near 100 km. The large signal-to-noise level is a consequence of both the quality of the SABER instrument and the intensity of the $\Delta v = 2$ transitions of the OH molecule which are its strongest as evidenced by Einstein A coefficients exceeding $100 \, s^{-1}$ (see Table 1).

[23] The derivation of atomic oxygen from the OH 2.0 μm emission requires inversion of the measured limb radiance to a vertical profile of volume emission rate. The limb radiance
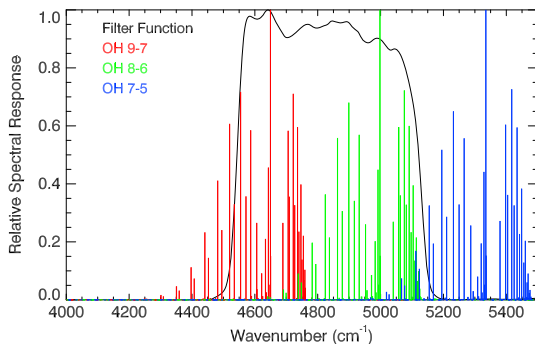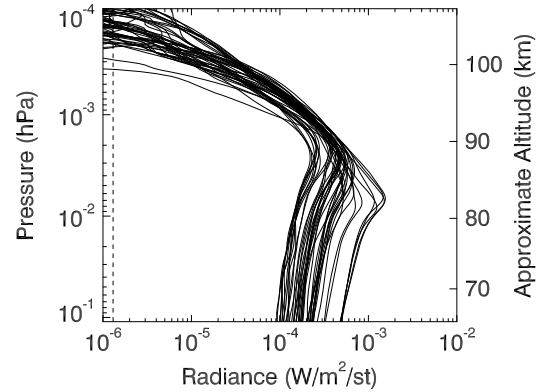
is inverted using an Abel inversion that is based on the assumption that the OH emission is in the weak line radiative transfer limit. The initial inversion provides the emission rate weighted by the spectral response function shown in Figure 6. To get the total band emission rate for the sum of the 9–7 and 8–6 bands, an "unfilter" factor is applied to the retrieved in-band emission rate. This factor is the ratio of the total emission rate to the in-band emission rate computed from simulations of the OH emission. For the 2.0 μm channel, the unfilter factor used in the operational SABER data processing is 1.10. The details of the derivation of the unfilter factor are given in *Mlynczak et al.* [2005]. Shown in Figure 8 is an example of a single 2.0 μm volume emission rate profile retrieved from an individual SABER limb radiance measurement. The profile displays the classic airglow shape in the mesopause region. The peak emission rate for this profile is about 5.6×10^4 photons $cm^{-3} \, s^{-1}$. Figure 9 shows the annual zonal average night volume emission rate (in ergs $cm^{-3} \, s^{-1}$, the standard SABER units for volume emission rate) for the sum of the OH(9–7) and OH(8–6) bands for 2004 in the mesopause region. The OH emission signals are quite large and readily facilitate the retrieval of the volume emission rate and hence the inference of atomic oxygen. As with ozone, the vertical resolution of the OH emission rates is approximately 2 km.

[24] To derive atomic oxygen at night, it is assumed that the production of ozone by recombination is balanced by loss of ozone through reaction with atomic hydrogen (H), i.e.,

$$k_4 \, [H] \, [O_3] \quad = \quad k_2 \, [O] \, [O_2] \, [M] \qquad (2)$$

[25] In equation (2), k_4 is the rate coefficient for the reaction of H and O_3; the reaction produces vibrationally excited OH in the $v = 9$, 8, 7, and 6 states. Because SABER observes the 9–7 and 8–6 emission, it is only necessary to construct a model of the emission from the $v = 9$ and $v = 8$ states. The OH emission intensity observed by SABER is directly proportional to the product $k_4 \, H \, O_3$, and thus, the emission intensity is directly proportional to the O-atom concentration via equation (2).

Figure 6. SABER OH 2.0 μm relative spectral response function and normalized line strengths for the 9–7, 8–6, and 7–5 bands.

Table 1. SABER OH Model Parameters Used in Derivation of Atomic Oxygen at Night

Symbol	Process Description	Rate Coefficient Value
f_9	Fraction of OH formed in $v=9$ state	0.4444
f_8	Fraction of OH formed in $v=8$ state	0.2756
A_9	Inverse radiative lifetime of OH $v=9$	$215.05\,\mathrm{s}^{-1}$
A_8	Inverse radiative lifetime of OH $v=8$	$178.06\,\mathrm{s}^{-1}$
A_{98}	Einstein coefficient for $v=9$ to $v=8$ transition	$20.05\,\mathrm{s}^{-1}$
A_{97}	Einstein coefficient for $v=9$ to $v=7$ transition	$118.35\,\mathrm{s}^{-1}$
A_{86}	Einstein coefficient for $v=8$ to $v=6$ transition	$117.21\,\mathrm{s}^{-1}$
$k9o2$	Rate coefficient for removal of $v=9$ in collisions with O_2	$1.05 \times 10^{-11}\,\exp(220/T)\,\mathrm{cm^3\,s^{-1}}$
$k9n2$	Rate coefficient for removal of $v=9$ in collisions with N_2	$3.36 \times 10^{-13}\,\exp(220/T)\,\mathrm{cm^3\,s^{-1}}$
$k9o$	Rate coefficient for removal of $v=9$ in collisions with O	$5 \times 10^{-11}\,\mathrm{cm^3\,s^{-1}}$
C_9	Sum of $k9o2$, $k9n2$, $k9o$	
$k8o2$	Rate coefficient for removal of $v=8$ in collisions with O_2	$8 \times 10^{-12}\,\mathrm{cm^3\,s^{-1}}$
$k8n2$	Rate coefficient for removal of $v=8$ in collisions with N_2	$7 \times 10^{-13}\,\mathrm{cm^3\,s^{-1}}$
$k8o$	Rate coefficient for removal of $v=8$ in collisions with O	$5 \times 10^{-11}\,\mathrm{cm^3\,s^{-1}}$
C_8	Sum of $k8o2$, $k8n2$, $k8o$	
$k98o2$	Rate coefficient for quenching $v=9$ to 8 in collisions with O_2	$4.2 \times 10^{-12}\,\mathrm{cm^3\,s^{-1}}$
$k98n2$	Rate coefficient for quenching $v=9$ to 8 in collisions with N_2	$4.0 \times 10^{-13}\,\mathrm{cm^3\,s^{-1}}$
C_{98}	Sum of $k98o2$, $k98n2$	

[26] At night, ozone is also lost by reaction with atomic oxygen, although this mechanism is approximately 10–20 times smaller than loss by reaction with atomic hydrogen (i.e., it is 5%–10% of the total loss of ozone at night). It is possible in principle to include this mechanism in the SABER algorithm. However, including this mechanism often resulted in nonphysical O values, particularly near 80 km at night where the O-atom concentration is extremely small. This mechanism is neglected in the SABER operational algorithms and results in an additional small uncertainty in the derived atomic oxygen at night.

[27] The SABER model for deriving night atomic oxygen includes production of OH in the $v=9$ and 8 states, spontaneous emission of radiation, and physical quenching by N_2, O_2, and O. The measured SABER OH volume emission rate, V (photons cm^{-3} s^{-1}), is given by the following expression:

$$V = P\left[\frac{f_9}{A_9 + C_9}A_{97} + \frac{f_8}{A_8 + C_8}A_{86} + \frac{f_9}{A_9 + C_9}\frac{A_{98} + C_{98}}{A_8 + C_8}A_{86}\right] \quad (3)$$

[28] In equation (3), P is the rate of reaction of k_4 H O_3 that is set equal to the rate k_2 O O_2 M, which enables the derivation of atomic oxygen, following the technique of

Good [1976]. SABER temperature and pressure data are used in the evaluation of k_2 and the calculation of O_2 (mixing ratio of 0.21) and M via the ideal gas law.

[29] In equation (3), A_9 and A_8 are the inverse radiative lifetimes (s^{-1}) of the $v=9$ and 8 states, respectively, i.e., the sum of the inverse lifetimes for transitions to all states below them. A_{98}, A_{97}, and A_{86} are state-specific transitions for the 9→8, 9→7, and 8→6 transitions, respectively. The terms f_9 and f_8 are the quasi-nascent distributions, that is, the fraction of OH formed in the $v=9$ and 8 states, respectively. The terms C_9 and C_8 represent the total rates (s^{-1}) of loss from the $v=9$ and 8 states due to collisional processes, including chemical reactions, with N_2, O_2, and O. C_{98} is the rate for quenching of the $v=9$ to the $v=8$ state by collisions. As can be seen in equation (3), the SABER atomic oxygen depends largely on total rates of loss from the $v=9$ and 8 states and on state-to-state rate coefficients. In addition, there are a relatively small number of parameters in the SABER model of night OH emission. Thus, the SABER approach has two advantages: SABER observes OH immediately upon its formation and requires only a small number of kinetic and spectroscopic parameters to model the OH emission. Equation (3) may be solved for atomic oxygen as
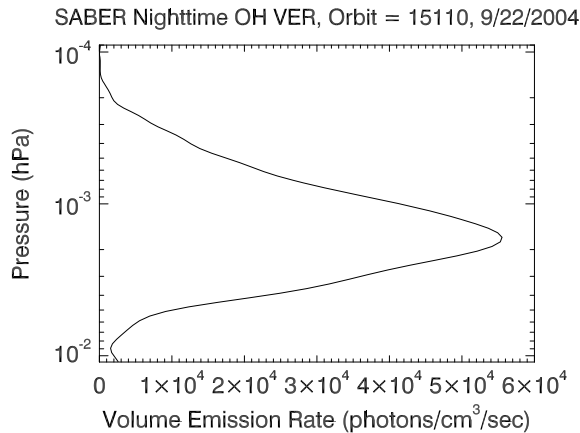
Figure 8. Example of an individual SABER 2.0 μm volume emission rate profile measured on 22 September 2004.
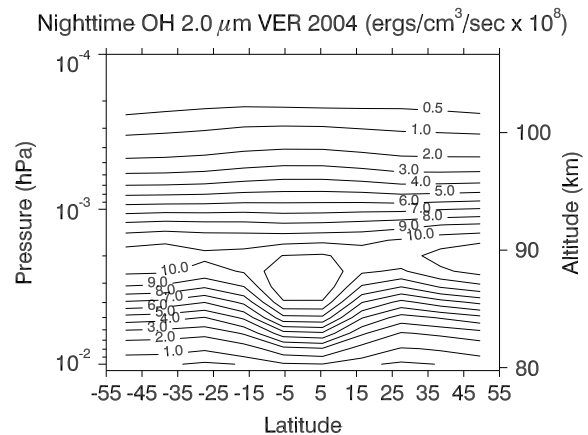
Figure 9. SABER annual zonal average 2.0 μm volume emission rate profile (erg cm^{-3} s^{-1}) for 2004.

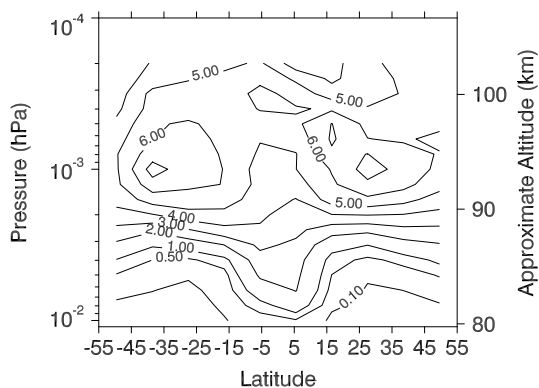**Figure 10.** SABER zonal average night atomic oxygen concentration for 22 September 2004.

a function of the measured volume emission rate V and the kinetic and spectroscopic parameters. Because atomic oxygen appears in the quenching of OH(v) (the C terms in equation (3)), the actual solution for atomic oxygen is in the form of a quadratic equation.

[30] The rate coefficients used in the operational SABER night algorithm are given in Table 1. The quasi-nascent pumping fractions f_9 and f_8 are from *Klenerman and Smith* [1987]. The Einstein *A* coefficients and inverse radiative lifetimes A_9 and A_8 are computed from the OH dipole measurements of *Nelson et al.* [1990] and are consistent with the results of *Goldman et al.* [1998] and with recent theoretical studies of *van der Loo and Groenenboom* [2007]. A member of the *Nelson et al.* [1990] group provided these values to the SABER team early on in the project (D. Nesbitt, Joint Institute for Laboratory Astrophysics, private communication, 1995). The Einstein coefficients reported in the HITRAN database of IR spectral line parameters [*Rothman et al.*, 2009] are taken from *Goldman et al.* [1998]. The *A* values for the 9–7 and 8–6 transitions computed by the SABER science team using the HITRAN database are within 6% of the values reported in Table 1. The values A_{97} and A_{86} are quite large and account for the large radiative signals from the OH bands measured by SABER.

[31] The physical quenching rates in Table 1 are from *Adler-Golden* [1997] and are included for collisions between OH(v) and N_2 and O_2. As with spontaneous emission, the total rate of loss from the $v = 9$ and 8 states is the dominant collisional parameter in the SABER model. Physical quenching is dominated by collisions with molecular oxygen. The temperature dependence of the rates k9o2 and k9n2 in Table 1 were suggested by K. Kalogerakis (SRI International, private communication, 2008) and are included in the SABER OH model.

[32] An important consideration is the rate of physical quenching or chemical reaction of highly vibrationally excited OH with O. The reaction of atomic oxygen with ground-state OH proceeds at a relatively fast rate, with a rate coefficient of $\sim 4 \times 10^{-11}$ cm^3 s^{-1} at mesopause region temperatures. There have been several papers in the literature over the years reporting values for the reaction/quenching/removal of OH(v) in collisions with O. Most recently, *Kalogerakis et al.* [2011] reported a value for removal of

OH($v = 9$) by O of $\sim 4 \times 10^{-10}$ cm^3 s^{-1}. This value is approximately 1 order of magnitude larger than the reaction rate of ground-state OH with O and is comparable to the classical gas kinetic rate for collisional processes. Because of the potential importance of this rate coefficient, we devote the next section to it. We will show that the retrieved atomic oxygen is highly dependent on whether the deactivation of OH($v = 9$) in collisions with O proceeds by single quantum step deactivation to $v = 8$ or by reaction. The reactive pathway will be shown to yield physically unrealistic O-atom amounts and nonphysical heating rates due to the recombination of atomic oxygen.

[33] Figure 10 shows night zonal average atomic oxygen concentrations on 22 September 2004, between 0.01 and 0.0001 hPa, derived from SABER measurements using the expression in equation (3) and the rate coefficients in Table 1. Peak night concentrations of $\sim 7 \times 10^{11}$ cm^{-3} occur near 95 km altitude on this day. These night zonal average values compare quite well with the day zonal averages shown in Figure 3 both in magnitude and in the location of the altitude/pressure at which the peak concentration occurs. Figure 11 shows the night zonal annual average atomic oxygen concentration as a function of pressure and approximate altitude. Peak O-atom concentrations between 6 and 6.5×10^{11} cm^{-3} occur near 95 km altitude. These again compare well with the annual zonal daytime atomic oxygen concentrations shown in Figure 4, although there is clearly a "two cell" feature evident in the night data. Figure 12 compares the global annual average atomic oxygen concentrations for day and night in 2004. The global annual average is computed by taking the average of the zonal annual profiles of atomic oxygen shown in Figures 4 and 11, weighted by the cosine of the latitude. The peak concentration occurs near 95 km at approximately 6×10^{11} cm^{-3}. Also evident in Figure 12 is the nonzero atomic oxygen concentration in the daytime mesosphere below 80 km, while the night atomic oxygen is essentially zero there.

[34] The agreement between the day and night O in Figures 4 and 10 (daily zonal average), Figures 5 and 11 (annual zonal average), and Figure 12 (global annual average) is remarkable considering that the day and night atomic oxygen are derived from two completely independent techniques based on different photochemical relations and in-
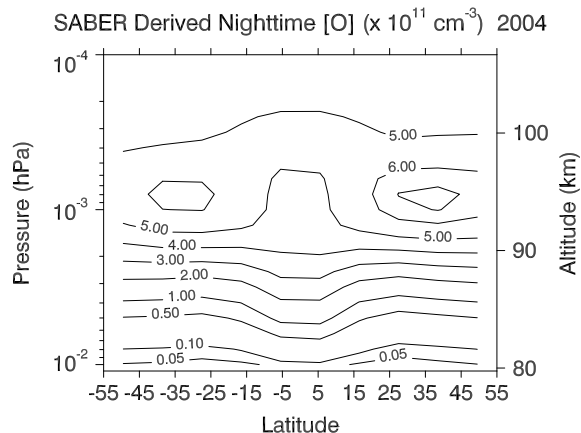

Figure 11. SABER annual zonal average night atomic oxygen concentration for 2004.
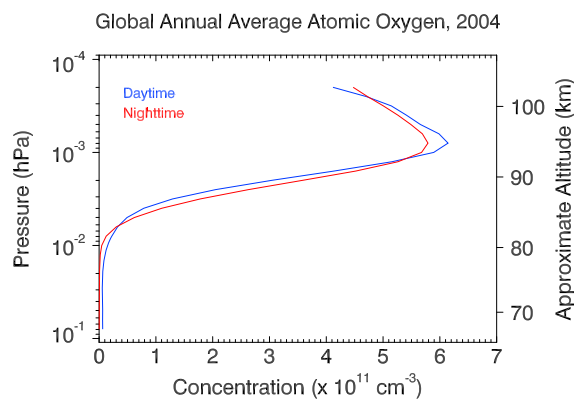
Figure 12. SABER day and night global annual average atomic oxygen concentrations for 2004.

volve measurements of different IR emissions, both of which are in non-LTE. The day and night retrieval algorithms share only the rate coefficient k_2 for recombination of O and O_2. The day and night consistency, especially over long time frames, gives high confidence that the SABER atomic oxygen is representative of the O-atom concentrations in the MLT.

4. Effect of Collisions Between O and Highly Vibrationally Excited OH

[35] Quenching of vibrationally excited OH in collisions with atomic oxygen may be important in the derivation of O-atom concentrations from measurements of OH emission by SABER. The basic concept is that the rate of reaction and/or quenching of OH(v) by atomic oxygen could be larger than the reaction rate with ground-state OH. At room temperature, the reaction rate coefficient for $OH + O \rightarrow O_2 + H$ is 3.3×10^{-11} cm^3 s^{-1} [*Sander et al.*, 2011]. *Spencer and Glass* [1977] reported a room temperature deactivation rate of OH(1) in collisions with O of 10.5×10^{-11} cm^3 s^{-1}. *Perminov et al.* [1998] derived from nightglow measurements a rate coefficient of 22×10^{-11} cm^3 s^{-1} for the rate of quenching of each OH(v) level by O. *Khachatrian and Dagdigian* [2005] measured in the laboratory a rate coefficient of 3.9×10^{-11} cm^3 s^{-1} for quenching of OH(1) by O. Most recently, *Kalogerakis et al.* [2011] reported laboratory measurements of the rate coefficient for the removal of the $v = 9$ and 8 states through collisions with O of 40×10^{-11} cm^3 s^{-1} for quenching of the $v = 9$ state and 30×10^{-11} cm^3 s^{-1} for the $v = 8$ state. The *Kalogerakis et al.* [2011] rate coefficients are comparable to the classic gas kinetic limit for neutral particle collisions and are the result of several years of very difficult laboratory measurements. They are the largest rate coefficients for OH(v)-O collisions reported to date.

[36] As noted in Table 1, the SABER operational algorithm presented here incorporates rate coefficients for removal of OH(9) and OH(8) by O that are factors of 8 and 6 smaller than the results reported in the *Kalogerakis et al.* [2011] paper. The SABER algorithm presumes that collisions between OH(9) and OH(8) proceed entirely by chemical reaction. Different rate coefficients and mechanisms (e.g., quenching to lower vibrational states) can be readily incorporated in the SABER

algorithm to test their influence on the derived O-atom concentration. The key question for the SABER algorithm is what is the result of the collision between OH(9) and O? There are two options: complete removal by OH(9), either through reaction or quenching to a vibrational state below $v = 8$, or complete quenching to OH(8) in a single quantum step. In the language of *McDade* [1991], does the process proceed by "sudden death" or single-step relaxation?

[37] To assess the effects of large rates of quenching of OH(9) and OH(8) by O on the retrieved SABER atomic oxygen, we used the *Kalogerakis et al.* [2011] rates in the SABER algorithm in three case studies: (1) complete removal of OH(9) in collisions with O, (2) a single quantum step from OH(9) to OH(8), and (3) 50% removal and 50% single-step quenching. Shown in Figure 13 are the night global annual mean O-atom concentrations for 2004 for the SABER baseline algorithm (red curve), for the complete reaction of OH(9) with O (case 1, black curve), for complete quenching of OH(9) to OH(8) in collisions with O (case 2, blue curve), and for 50% removal, 50% single-step quenching (case 3, green curve). The SABER baseline case (red curve, rates from Table 1) and case 2 are nearly identical, with peak concentrations between 5.5 and 6 $\times$ 10^{11} cm^{-3}. Cases 1 and 3, in which collisions between OH (9) and O result in full or partial reaction, have substantially larger atomic oxygen concentrations, peaking at 8.5 and 20×10^{11} cm^{-3}, respectively.

[38] Because of the difficulty of measuring atomic oxygen directly in the Earth's upper MLT, it is necessary to resort to other means to assess the validity of the O-atom amounts inferred from the SABER (and other) techniques. A very clear approach is afforded by the role O plays in the energy budget of the upper MLT. Specifically, the recombination of
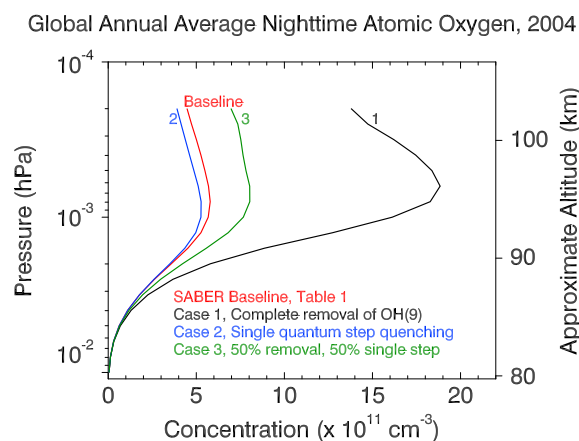
Figure 13. Night global annual mean atomic oxygen concentration for SABER baseline model (Table 1 and Figure 12) shown by the red line. Case 1 shows atomic oxygen derived when OH(9) is removed completely upon collision with O, case 2 when OH(9) is completely relaxed to OH(8) in collisions with O, and case 3 when there is a 50/50 split between complete removal of OH(9) and quenching of OH(9). Cases 1–3 use the large values for collisions between highly vibrationally excited OH and O reported by *Kalogerakis et al.* [2011].

Figure 14. Night global annual average heating rates (K/d) due to the recombination of atomic oxygen that correspond to the atomic oxygen concentrations shown in Figure 13. The heating rates for cases 1 and 3 are comparable to or larger than the radiative cooling rates in the mesopause region and are considered nonphysical. See text for full discussion.

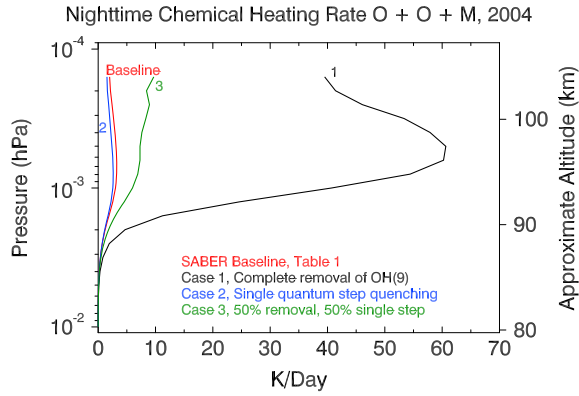atomic oxygen is a substantial source of heating in the upper MLT, and it is straightforward to compute the associated heating rate. The instantaneous heating rate due to the recombination of atomic oxygen, one of seven exothermic chemical reactions critical to the heat budget of the mesopause, is given by the following:

$$\frac{\partial T}{\partial t} = \frac{2}{7} \frac{1}{k_b} k_1 [O] [O] \Delta H \qquad (4)$$

[39] In this equation, k_b is Boltzmann's constant, k_1 is the rate coefficient for recombination of atomic oxygen, and ΔH is the enthalpy of reaction. A key point about equation (4) is that the heating due to recombination of atomic oxygen

is proportional to the square of the O-atom concentration. The heating rate due to this reaction will quickly become very large as the atomic oxygen concentration increases.

[40] Figure 14 shows the night global annual average heating rates due to the recombination of atomic oxygen for 2004 for the O-atom concentrations in Figure 13. These are computed using each profile of atomic oxygen measured by SABER in 2004 (approximately 400,000 profiles) between $\pm 55°$ latitude, each weighted by the cosine of the latitude. As noted in section 1.1, the baseline SABER processing screens out O-atom concentrations larger than $1.25 \times 10^{12}\,\text{cm}^{-3}$. This screening process eliminated less than 2% of the data between 0.01 and 0.0001 hPa. To accommodate the larger rate coefficients for quenching of OH(9) and OH (8) by O, the value of the screen was increased by a factor of 10, to $1.25 \times 10^{13}\,\text{cm}^{-3}$. This resulted in less than 3% of the total data being eliminated. The SABER baseline results peak at about 3.5 K/d, while the heating rates obtained for case 1 peak at over 60 K/d. As would be expected, case 2 has chemical heating rates nearly identical to the SABER baseline case, while case 3 peaks at about 10 K/d.

[41] As we will show in Paper 2, global annual mean radiative cooling by CO_2 as derived from SABER measurements is about 15 K/d at the altitude of the peak of the O-atom concentration. Thus, the heating rates for case 1 are approximately a factor of 5 larger than the observed cooling rates. The chemical heating rates for case 3 are comparable to the CO_2 radiative cooling rates. The atomic oxygen concentrations from both of these cases can be rejected as nonphysical because they signify a permanent imbalance of excess heating over cooling in the mesopause region. The SABER baseline case and case 2 (single-step quenching of OH(9) to OH(8) in collisions with O) both yield atomic oxygen concentrations that, when all other chemical and solar heating terms are considered, will be in approximate balance with the observed global annual cooling rates. It is suggested that further laboratory measurements and theoretical

Table 2. Estimated Uncertainty in Night Atomic Oxygen Derived From SABER OH Measurements

Parameter	f9p	f8p	k9o2	k8o2	kr	A_{86}	RSS
Uncertainty	(+0.03)	(+0.03)	1.25	1.25	1.2	1.1	
Pressure (hPa)							
1.00E-04	−1.97	−2.24	0.79	0.20	−9.35	−2.35	10.85
1.26E-04	−3.06	−3.47	1.37	0.37	−14.32	−3.69	16.83
1.58E-04	−3.53	−4.12	1.91	0.52	−16.01	−4.37	18.97
2.00E-04	−3.58	−4.30	2.50	0.70	−16.40	−4.57	19.51
2.51E-04	−3.49	−4.34	3.01	0.90	−16.48	−4.62	19.57
3.16E-04	−3.60	−4.60	3.62	1.17	−16.98	−4.91	20.29
3.98E-04	−3.69	−4.85	4.21	1.49	−17.39	−5.20	20.90
5.01E-04	−3.66	−4.98	4.72	1.81	−17.57	−5.35	21.20
6.31E-04	−3.62	−5.06	5.22	2.21	−17.59	−5.46	21.36
7.94E-04	−3.56	−5.12	5.61	2.63	−17.55	−5.57	21.44
1.00E-03	−3.49	−5.16	6.07	3.15	−17.49	−5.64	21.54
1.26E-03	−3.48	−5.27	6.50	3.74	−17.50	−5.80	21.79
1.58E-03	−3.45	−5.38	7.02	4.47	−17.53	−5.97	22.14
2.00E-03	−3.39	−5.43	7.34	5.18	−17.37	−6.06	22.25
2.51E-03	−3.31	−5.44	7.62	5.94	−17.20	−6.11	22.37
3.16E-03	−3.25	−5.45	7.85	6.67	−17.05	−6.17	22.51
3.98E-03	−3.18	−5.43	8.03	7.34	−16.94	−6.18	22.66
5.01E-03	−3.17	−5.46	8.25	8.04	−16.88	−6.25	22.96
6.31E-03	−3.11	−5.46	8.37	8.70	−16.78	−6.28	23.16
7.94E-03	−3.06	−5.51	8.44	9.36	−16.72	−6.34	23.42
1.00E-02	−2.99	−5.59	8.43	10.02	−16.68	−6.42	23.70

modeling are required to determine the product states resulting from collisions between OH(9) and O.

[42] The above discussion strongly suggests that atmospheric energetics is a powerful tool that may be used to assess the validity and to constrain the O-atom concentration in the mesopause region. This topic is explored in detail in Paper 2 [*Mlynczak et al.*, 2013], in which principles of global mean energy balance may be used to derive a constraint on the global mean O-atom concentration, a situation made possible by the unique nature of the energy budget in the upper MLT.

5. Assessment of Uncertainty in Derived Atomic Oxygen

[43] The techniques used to derive atomic oxygen carry uncertainty associated with the use of kinetic, spectroscopic, and photochemical parameters necessary to model the non-LTE radiative emissions or to express chemical relationships. Given the general agreement shown above between the day and night global annual average O, it is instructive to consider the uncertainty in the O due to the parameters used in the derivations.

[44] The uncertainty in night atomic oxygen is assessed by perturbing the parameters listed in Table 1 by specified amounts and then examining the change in the global mean O from the baseline, unperturbed state. The parameters are assumed to be uncorrelated so that the total uncertainty in O due to the uncertainty in all parameters is obtained by computing the root-sum-square (RSS) of all of the individual changes in the global mean O. This approach provides the one standard deviation ("1 − sigma") uncertainty and has been used to assess uncertainty in several SABER-related data products [e.g., *Mlynczak and Olander*, 1995; *Mertens et al.*, 2001]. For this exercise, all A values are perturbed by 10%; all collisional quenching rates are perturbed by 25%; f_8 and f_9 are changed by 0.03 each, which corresponds to the uncertainty of f_8 specified in *Klenerman and Smith* [1987]; and the recombination rate coefficient k_2 is perturbed by 20% based on the uncertainty at a temperature of 200 K calculated from the error expression for this coefficient found in the JPL 2011 handbook [*Sander et al.*, 2011].

[45] The results are listed in Table 2 as a function of pressure for parameters that provide the six largest sources of uncertainty. The total uncertainty is shown in the rightmost column and includes the uncertainty in all parameters in Table 1. The single largest uncertainty overall is due to the rate coefficient for the recombination of O and O_2 which occurs due to the assumption of photochemical balance (equation (2)) and is specifically the term "P" in equation (3). The overall uncertainty in the SABER night atomic oxygen is estimated to be less than 25%.

[46] The uncertainty in daytime atomic oxygen is assessed from equation (1). The parameters are the ozone mixing ratio, the ozone Hartley band photolysis rate, the O_2 density, the total number density, and the rate coefficient for the recombination of O_2 and O. A formal uncertainty analysis has not yet been carried out on the SABER ozone derived from 9.6 μm in the upper MLT. For the present purpose, we estimate this uncertainty at ~20%, which when combined with the previously stated uncertainty of 20% for k_2 results in a daytime atomic oxygen uncertainty of ~30% in the MLT region. Uncertainties in the photolysis rate, temperature,

and density are not significant in the total uncertainty budget. Radiometric calibration of SABER is not a major source of uncertainty for day or night. Random error resulting from radiance noise is typically less than 10% for an individual profile based on the radiance data shown in Figures 2 and 7, but it rapidly becomes inconsequential through averaging to zonal or global means on daily or longer time scales.

6. Summary, Discussion, and Conclusion

[47] We have presented the algorithms used to derive atomic oxygen in the Earth's MLT region from observations made by the SABER instrument on the TIMED satellite. Two different and independent techniques are employed: in the day, measurements of ozone are used under the assumption of photochemical balance between recombination of O and O_2 and photolysis of O_3; at night, the OH Meinel band emission is used under the assumption of photochemical balance between recombination of O and O_2 and reaction of H and O_3. Both techniques yield atomic oxygen amounts for daily zonal averages, annual zonal averages, and annual global averages that are in close agreement despite proceeding from completely independent measurements and application of different non-LTE rate coefficients. Peak atomic oxygen concentrations of approximately 6.0–6.5 $\times 10^{11}$ cm^{-3} are found near 8×10^{-4} hPa (~95 km).

[48] We also examined the role of collisions between O and highly vibrationally excited OH and the effect of recently reported large rate coefficients on the derived SABER atomic oxygen. We find that the SABER results do not support a large value for reaction of OH(9) and atomic oxygen. However, if the collision results in deactivation of OH (9) completely to OH(8), then atomic oxygen concentrations consistent with the operational SABER algorithm are realized. We suggested that the validity of derived atomic oxygen could be determined by examining the heat liberated by the recombination of oxygen atoms, relative to the radiative cooling of the mesopause region. This concept is further explored in Paper 2. Further research into the product states of collisions between OH(9) and OH(8) and O appears warranted from the results presented here. The excellent SABER radiances and retrieved volume emission rates should play a central role in any such study. Because the derivation of O involves use of numerous rate coefficients and parameters, we estimated the uncertainty of the O and found it to be less than 30% during day and less than 25% at night. The rate coefficient for recombination of O and O_2 is the largest source of uncertainty in both derivations.

[49] As noted by *Smith et al.* [2010], the baseline SABER atomic oxygen is larger than that derived from other satellite measurements such as those from the WINDII instrument [*Russell et al.*, 2005]. The SABER O-atom results also appear at times to be larger than those derived from the OSIRIS instrument [*Sheese et al.*, 2011], although the night concentrations shown in Figure 11 of *Sheese et al.* [2011] at 90 km appear to be quite similar in magnitude to those shown in Figure 10 of this paper. Both the WINDII and OSIRIS atomic oxygen concentrations are, like SABER's, derived from observations of airglow/non-LTE emission intensities. A comparison of SABER, OSIRIS, and WINDII atomic oxygen will be reported in a future paper.
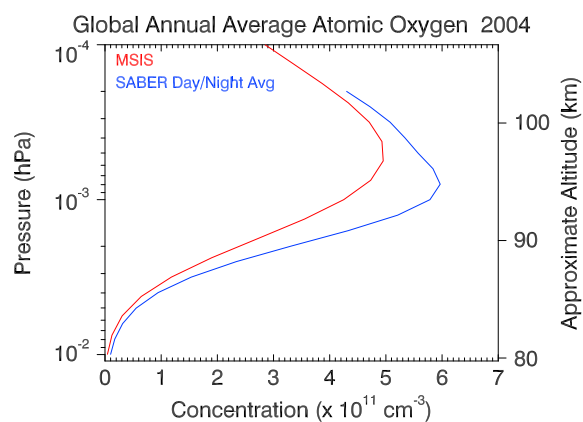
Global Annual Average Atomic Oxygen 2004

Figure 15. Comparison of MSIS and SABER global annual mean atomic oxygen concentrations for 2004. The mean is computed between $\pm 55°$ latitude as described in the text.

[50] SABER atomic oxygen is also larger than that given by the MSIS empirical model [*Picone et al.*, 2002]. Shown in Figure 15 is a comparison between SABER and MSIS global annual mean atomic oxygen for the year 2004 between $\pm 55°$ latitude. The MSIS peak concentration is at a higher altitude than SABER observes and MSIS O is smaller. However, some of the discrepancy in magnitude is due to a 25% decrease in MSIS O between the equator and $55°$ latitude. No such gradients are observed in SABER, day or night. Between $\pm 33°$ latitude, the agreement between SABER and MSIS is much better than that shown in Figure 15, although SABER is still larger.

[51] The OH collisional quenching rates would have, in general, to decrease significantly from those reported in Table 1 to achieve a reduction in the SABER atomic oxygen. In addition, the SABER daytime ozone abundance would have to decrease in direct proportion to the decrease in night atomic oxygen in order to keep the day/night consistency within the SABER data set. Decreasing the daytime ozone requires a decrease in the collisional quenching rates used in the statistical equilibrium model for ozone vibrational states described in section 2. This discussion points out the need for an independent validation of the atomic oxygen concentration. As discussed above, the unique nature of the mesopause region energy budget affords this validation based on energy balance considerations and is the subject of the next paper [*Mlynczak et al.*, 2013].

[52] The SABER atomic oxygen record now exceeds 11 years in length with nearly 5 million individual vertical profiles of atomic oxygen. The algorithms described herein are available to the community and may be obtained by contacting the lead author of this paper.

References

Adler-Golden, S. (1997), Kinetic parameters for OH nightglow modeling consistent with recent laboratory measurements, *J. Geophys. Res.*, *102*(A9), 19,969–19,976, doi:10.1029/97JA01622.

Dickinson, P. H. G., R. C. Bolden, and R. A. Young (1974), Measurement of atomic oxygen in the lower ionosphere using a rocket-borne resonance lamp, *Nature*, *252*, 289–291.

Dickinson P. H. G., W. C. Bain, L. Thomas, E. R. Williams, D. B. Jenkins, and N. D. Twiddy (1980), The determination of the atomic oxygen concentration and related parameters in the lower ionosphere, *Proc. R. Soc. A.*, *369*, 379–408, doi:10.1098/rspa.1980.0006.

Goldman A, W. G. Schoenfeld, D. Goorvitch, C. Chackerian, H. Dothe, F. Mélen, M. C. Abrams, J. E. A. Selby (1998), Updated line parameters for OH $X^2\Pi$–$X^2\Pi$ (ν'', ν') transitions, *J. Quant. Spectrosc. Radiat. Transfer*, *59*, 453–469.

Good, R. E. (1976), Determination of atomic oxygen density from rocket borne measurements of hydroxyl airglow, *Planet. Space Sci.*, *24*, 389–395.

Grossmann, K. U., and K. Vollmann (1997), Thermal infrared measurements in the middle and upper atmosphere, *Adv. Space Res.*, *19*, 631–638.

Grossmann, K. U., M. Kaufmann, and E. Gerstner (2000), A global measurement of lower thermosphere atomic oxygen densities, *Geophys. Res. Lett.*, *27*(9), 1387–1390, doi:10.1029/2000GL003761.

Kalogerakis, K. S., G. P. Smith, and R. A. Copeland (2011), Collisional removal of OH ($X^2\Pi$, $v=9$) by O, O_2, O_3, N_2, and CO_2, *J. Geophys. Res.*, *116*, D20307, doi:10.1029/2011JD015734.

Khachatrian, A., and P. J. Dagdigian (2005), Vibrational relaxation of OH by oxygen atoms, *Chem. Phys. Lett.*, *415*, 1–5.

Klenerman, D., and I. W. M. Smith (1987), Infrared chemiluminescence studies using a SISAM spectrometer, *J. Chem. Soc. Faraday Trans. 2*, 83,229–241, doi:10.1039/F29878300229.

Llewellyn, E. J. (1988), The concentration of atomic oxygen in the mesosphere and thermosphere, *Planet. Space Sci.*, *36*, 892.

Marsh, D. R., A. K. Smith, M. G. Mlynczak, and J. M. Russell III (2006), SABER observations of the OH Meinel airglow variability near the mesopause, *J. Geophys. Res.*, *111*, A10S05, doi:10.1029/2005JA011451.

Martin-Torres, F. J. (1999), Emisiones Infrarrojas del Ozono en la Atmosfera de la Tierra, PhD thesis, Univ. de Granada, Granada, Spain.

McDade, I. C. (1991), The altitude dependence of the OH ($X^2\Pi$) vibrational distribution in the nightglow: Some model expectations, *Planet. Space Sci.*, *39*(A7), 1049–1057.

McDade, I. C., and E. J. Llewellyn (1987), Kinetic parameters related to sources and sinks of vibrationally excited OH in the nightglow, *J. Geophys. Res.*, *92*, 7643–7650.

McDade, I. C., E. J. McLlewellyn, D. P. Murturgh, and R. G. H. Greer (1987), ETON 5: Simultaneous rocket measurements of the OH Meinel ($\Delta v=2$ sequence and (8, 3) band emission profiles in the nightglow, *Planet. Space Sci.*, *35*, 1137–1147.

Menard-Bourcin, F., J. Menard, and L. Doyennette (1991), Vibrational relaxation of ozone in O_3-O_2 and O_3-N_2 gas mixtures from infrared double-resonance measurements, *J. Chem. Phys.*, *94*, 1875.

Mertens, C. J., M. G. Mlynczak, M. López-Puertas, P. P. Wintersteiner, R. H. Picard, J. R. Winick, L. L. Gordley, and J. M. Russell III (2001), Retrieval of mesospheric and lower thermospheric kinetic temperature from measurements of CO_2 15 μm Earth limb emission under non-LTE conditions, *Geophys. Res. Lett.*, *28*(7), 1391–1394, doi:10.1029/2000GL012189.

Mlynczak, M. G. (1999), A new perspective on the molecular oxygen and hydroxyl airglow emissions, *J. Geophys. Res.*, *104*(D22), 27, 535–27, 543, doi:10.1029/1999JD000839.

Mlynczak, M. G., and S. R. Drayson (1990a), Calculation of infrared limb emission by ozone in the terrestrial middle atmosphere: 1. Source functions, *J. Geophys. Res.*, *95*(16), 497–16, 511.

Mlynczak, M. G., and S. R. Drayson (1990b), Calculation of infrared limb emission by ozone in the terrestrial middle atmosphere: 2. Emission calculations, *J. Geophys. Res.*, *95*(16), 512–16, 521.

Mlynczak, M. G., and S. R. Drayson (1991), Rapid computation of the radiative absorption rate in the v3 mode of mesospheric and lower thermospheric ozone, *J. Quant. Spectrosc. Radiat. Transfer 46*(5), 463–471.

Mlynczak, M. G., and D. S. Olander (1995), On the utility of the molecular oxygen dayglow emissions as proxies for middle atmospheric ozone, *Geophys. Res. Lett.*, *22*(11), 1377–1380, doi:10.1029/95GL01321.

Mlynczak, M. G., and S. Solomon (1991), Middle atmosphere heating by exothermic chemical reactions involving odd-hydrogen species, *Geophys. Res. Lett.*, *18*(1), 37–40, doi:10.1029/90GL02672.

Mlynczak, M. G., and S. Solomon (1993), A detailed evaluation of the heating efficiency in the middle atmosphere, *J. Geophys. Res.*, *98*(D6), 10,517–10,541, doi:10.1029/93JD00315.

Mlynczak, M. G., F. J. Martin-Torres, D. G. Johnson, D. P. Kratz, W. A. Traub, and K. Jucks (2004), Observations of the O(^{3}P) fine structure line at 63 μm in the upper mesosphere and lower thermosphere, *J. Geophys. Res.*, *109*, A12306, doi:10.1029/2004JA010595.

Mlynczak, M. G., et al. (2005), Energy transport in the thermosphere during the solar storms of April 2002, *J. Geophys. Res.*, *110*, A12S25, doi:10.1029/2005JA011141.

Mlynczak, M. G., B. T. Marshall, F. J. Martin-Torres, J. M. Russell III, R. E. Thompson, E. E. Remsberg, and L. L. Gordley (2007), Sounding of the atmosphere using broadband emission radiometry observations of daytime mesospheric $O_2(^1\Delta)$ 1.27 μm emission and derivation of ozone,

atomic oxygen, and solar and chemical energy deposition rates, *J. Geophys. Res.*, *112*, D15306, doi:10.1029/2006JD008355.

Mlynczak, M. G., et al. (2013), Radiative and energetic constraints on the global annual mean atomic oxygen concentration in the mesopause region, *J. Geophys. Res.*, doi:10.1002/jgrd.50400.

Nelson, D. D., A. Schiffman, D. J. Nesbitt, J. J. Orlando, and J. B. Burkholder, H+O_3 Fourier-transform infrared emission and laser absorption studies of OH ($X^2\Pi$) radical: An experimental dipole moment function and state-to-state Einstein *A* coefficients, *J. Chem. Phys.*, *93*, 7003–7019, 1990.

Perminov, V. I., A. I. Semenov, and N. N. Shefov (1998), Deactivation of hydroxyl molecule vibrational states by atomic and molecular oxygen in the mesopause region, *Geomagn. Aeron.*, *38*, 761–764.

Picone, J. M., A. E. Hedin, D. P. Drob, and A. C. Aikin (2002), NRLMSISE-00 empirical model of the atmosphere: Statistical comparisons and scientific issues, *J. Geophys. Res.*, *107*(A12), 1468, doi:10.1029/2002JA009430.

Rothman, L. S., et al. (2009), The HITRAN 2008 molecular spectroscopic database, *J. Quant. Spectrosc. Radiat. Transfer*, *110*, 533–572, doi:10.1016/j.jqsrt.2009.02.013.

Rottman, G. (2005), The SORCE Mission, *Sol. Phys.*, *230*(1), 7–25.

Russell, J. M., M. G. Mlynczak, L. L. Gordley, J. Tansock, and R. Esplin (1999), An overview of the SABER experiment and preliminary calibration results, in *Proceedings of the 44th Annual Meeting, Denver, Colorado, July 18–23*, vol. *3756*, pp. 277–288, SPIE, Bellingham, WA.

Russell, J. P., W. E. Ward, R. P. Lowe, R. G. Roble, G. G. Shepherd, and B. Solheim (2005), Atomic oxygen profiles (80 to 115 km) derived from Wind Imaging Interferometer/Upper Atmospheric Research Satellite measurements of the hydroxyl and greenline airglow: Local time–latitude dependence, *J. Geophys. Res.*, *110*, D15305, doi:10.1029/2004JD005570.

Sander, S. P., et al. (2011), Chemical Kinetics and Photochemical Data for Use in Atmospheric Studies, Evaluation No. 17, JPL Publication 10-6, Jet Propulsion Laboratory, Pasadena, CA [Available at http://jpldataeval.jpl.nasa.gov.].

Sheese, P. E., I. C. McDade, R. L. Gattinger, and E. J. Llewellyn (2011), Atomic oxygen densities retrieved from Optical Spectrograph and Infrared Imaging System observations of O_2 A-band airglow emission in the mesosphere and lower thermosphere, *J. Geophys. Res.*, *116*, D01303, doi:10.1029/2010JD014640.

Siskind, D. E., and W. E. Sharp (1991), A comparison of measurements of the oxygen nightglow and atomic oxygen in the lower thermosphere, *Planet. Space Sci.*, *39*, 627–639.

Smith, A. K., D. R. Marsh, M. G. Mlynczak, and J. C. Mast (2010), Temporal variations of atomic oxygen in the upper mesosphere from SABER, *J. Geophys. Res.*, *115*, D18309, doi:10.1029/2009JD013434.

Solomon, S., J. T. Kiehl, B. J. Kerridge, E. E. Remsberg, and J. M. Russell III (1986), Evidence for nonlocal thermodynamic equilibrium in the ν_3 mode of mesospheric ozone, *J. Geophys. Res.*, *91*(D9), 9865–9876.

Spencer, J. E., and G. P. Glass (1977), Some reactions of OH($v=1$), *Int. J. Chem. Kinet.*, *9*, 111–122.

Ulwick, J. C., K. D. Baker, D. J. Baker, A. J. Steed, and W. R. Pendleton, Jr. (1987), Mesospheric minor species determinations from rocket and ground-based i.r. measurements, *J. Atmos. Sol. Terr. Phys.*, *49*, 855–862.

van der Loo, M. P. J., and G. C. Groenenboom (2007), Theoretical transition probabilities for the OH Meinel system, *J. Chem. Phys.*, *126*, 114314, doi:10.1063/1.2646859.

West, G. A., R. E. Weston Jr., and G. W. Flynn (1976), Deactivation of vibrationally excited ozone by O (3^P) atoms, *Chem. Phys. Lett.*, *42*, 488–493.

Xu, J., H. Gao, A. K. Smith, and Y. Zhu (2012), Using TIMED/SABER nightglow observations to investigate hydroxyl emission mechanisms in the mesopause region, *J. Geophys. Res.*, *117*, D02301, doi:10.1029/2011JD016342.